INDEX COPERNICUS INTERNATIONAL

Bio-Algorithms and Med-Systems

WWW.BAMSJOURNAL.COM ISSN: 1896-530X

ORIGINAL ARTICLE

**Received:** 11.12.2025
**Accepted:** 29.12.2025
**Published:** 31.12.2025

**CITE THIS ARTICLE AS:**
Kasperska K, Skurzok M, Moskal P, "Studies of Attenuation Effects in Two- and Three-Photon Positronium Decays in Phantom Models," Bio-Algorithms and Med-Systems vol. 21, special issue New Trends in Nuclear and Medical Physics, pp. 42-51, 2025, DOI: 10.5604/01.3001.0055.5414

**AUTHORS' CONTRIBUTION:**
**A** – Conceptualization
**B** – Data Curation
**C** – Formal Analysis
**D** – Funding Acquisition
**E** – Investigation
**F** – Methodology
**G** – Project Administration
**H** – Resources
**I** – Software
**J** – Supervision
**K** – Validation
**L** – Visualization
**M** – Writing – Original Draft
**N** – Writing – Review & Editing

**CORRESPONDING AUTHOR:**
Kamila Kasperska MSc; Faculty of Physics, Astronomy and Applied Computer Science, Jagiellonian University; S. Łojasiewicza street 11, 30-348 Kraków, Poland; E-mail: kamila.kasperska@doctoral.uj.edu.pl



# Studies of Attenuation Effects in Two- and Three-Photon Positronium Decays in Phantom Models

Kamila Kasperska[1,2ABCEFGIKLMN], Magdalena Skurzok[1,2AEFGJKMN], Paweł Moskal[1,2ADEFGHJKMN]

[1]Faculty of Physics, Astronomy and Applied Computer Science, Jagiellonian University, Kraków, Poland
[2]Center for Theranostics, Jagiellonian University, Kraków, Poland

## ABSTRACT

**Objective:** Positron emission tomography (PET) enables non-invasive imaging of metabolic processes. Standard PET reconstructs radiotracer distribution using two back-to-back photons from electron-positron annihilation. However, about 0.3–0.5% of annihilations result in the creation of three photons. Three photons may be created in direct annihilation and in annihilation via the formation of metastable ortho-positronium carrying additional information not used by conventional PET. The Jagiellonian-PET (J-PET) detector allows us to use this information by applying positronium imaging based on the ortho-positronium (o-Ps) lifetime or the 3γ/2γ decay ratio. Accurate tomographic images require attenuation correction. This study investigates photon absorption in phantom models to form a basis for future attenuation maps for three-gamma decays.
**Methods:** Monte Carlo (MC) simulations in ROOT and Geant4 Application for Tomographic Emission (GATE) were performed for water sphere, cylinder, a simplified head model and the mesh50_XCAT phantom. Both para-positronium (p-Ps) and o-Ps decays were simulated as uniformly distributed sources. Absorption probabilities were calculated by checking whether any photon in a multiplet interacted within the phantom. Emission--point-specific absorption maps were generated for all models. Toy MC and GATE simulations showed good overall agreement.
**Results:** Photon triplets from o-Ps decays experienced higher absorption than photon pairs from p-Ps due to lower individual energies and higher attenuation. Absorption maps showed the dependence of photon survival probability on the decay location. In the mesh50_XCAT phantom, 24.9% of p-Ps pairs and 10.3% of o-Ps triplets escaped without interaction.
**Conclusions:** Gamma absorption depends strongly on positronium decay mode and location, with o-Ps events experiencing higher attenuation. The generated absorption maps provide the first step toward dedicated attenuation correction for three-gamma positronium imaging, enabling accurate reconstruction in novel 3γ/2γ positronium imaging technique. The study presented indicates that the absorption of 3γ in the head is only about 2.5 times higher than for 2γ, which is encouraging for further development of the 3γ/2γ rate ratio imaging.

## KEYWORDS

positronium, PET, J-PET, positronium imaging, multiphoton imaging, three-gamma imaging, medical imaging, attenuation correction

## LIST OF ABBREVIATIONS

**GATE** – Geant4 Application for Tomographic Emission
**J-PET** – Jagiellonian positron emission tomography scanner
**MC** – Monte Carlo
**o-Ps** – ortho-positronium
**PET** – positron emission tomography
**p-Ps** – para-positronium
**Ps** – positronium
**XCAT** – eXtended CArdiac-Torso phantom

## BRIEF DESCRIPTION OF THE WORK

This work investigates the absorption in human tissue of gamma quanta from para- (p-Ps) and ortho-positronium (o-Ps) decays, using both simplified phantom models and a detailed eXtended CArdiac-Torso (XCAT) human phantom. o-Ps, formed in electron--positron interactions in tissue, can decay into three photons, which carry additional information not captured by standard positron emission tomography (PET) devices. The Jagiellonian-PET (J-PET) detector, capable of multi-photon detection, can use this information for positronium imaging with o-Ps lifetime and $3\gamma/2\gamma$ decay ratio methods. By generating emission-point--specific absorption maps, this study serves as a basis for accurate attenuation correction in three-gamma imaging.

## INTRODUCTION

Positron emitted inside the human body during PET can either annihilate directly with an electron from the environment or form a metastable-electron-positron-bound state known as positronium (Ps). Positronium can exist in two spin configurations: the singlet state, known as p-Ps, and the triplet state, known as o-Ps, which in a vacuum predominantly decay into two- and three-gamma quanta, respectively [1]. However, in the tissue the properties of o-Ps, such as its lifetime and the fraction of decays into three photons, are strongly influenced by the tissue submolecular structure [2]. This dependence has led to the development of a new imaging technique known as positronium imaging [3–7].

Current state-of-the-art PET scanners are limited to registering only two-photon decays and are therefore unable to provide information necessary for positronium imaging methods, which require the simultaneous registration of multiple photons from the same decay [8]. However, the J-PET, capable of multi-photon detection, addresses this limitation by providing the missing information [9]. The J-PET collaboration is currently investigating two main techniques of positronium imaging: positronium lifetime imaging [7, 10–12] and the method based on the $3\gamma/2\gamma$ annihilation ratio [13, 14]. The former relies on radionuclides that emit an additional de-excitation photon (prompt) immediately following the $\beta^+$ decay, which provides information about the positronium formation time, and on the subsequent detection of the two photons resulting from positronium annihilation, which provides information about the time of its decay, allowing the measurement of positronium lifetime [12]. This imaging method is referred to as two-plus-one -gamma imaging.

The second technique, based on the $3\gamma/2\gamma$ ratio, involves the detection of annihilation events from both, two-photon and three--photon decays [13]. This method offers the advantage of not relying on the presence of a prompt gamma emitted during the decay of the radioisotope, enabling the use of a broader range of radiopharmaceuticals for PET imaging applications. The approach, which reconstructs spatial information from the o-Ps $\rightarrow 3\gamma$ annihilation events, is known as three-gamma imaging [14, 15]. After demonstration of the first positronium images [6, 7] and three-gamma images [14], both positronium lifetime imaging [16–28] and three-gamma imaging [15, 29–37] are currently undergoing rapid development.

A primary goal of both, conventional two-gamma and novel three--gamma PET imaging, is to reconstruct the spatial distribution of a radioactive tracer within the patient's body. However, the reconstruction is affected by several sources of inaccuracy, the most significant of which is the attenuation of gamma quanta in matter (such as human tissue). The attenuation leads to an underestimation of radiopharmaceutical concentration in deeper tissues. To compensate for this effect, attenuation correction must be applied. In the J-PET scanner, a CT-based attenuation correction for two-gamma imaging is employed [11, 38, 39]. However, the standard attenuation maps optimised for two photons with energies of 511 keV are insufficient for three-gamma imaging. Developing attenuation maps dedicated to three-photon detection is challenging due to the more complex three-body decay nature [40]. In the o-Ps $\rightarrow 3\gamma$ annihilation, the photons are emitted in a single plane with energies ranging from 0 to 510 keV, such that momentum and energy are conserved. Therefore, energy--dependent attenuation corrections are needed.

The aim of this work is to investigate the three- and two--gamma quanta absorption in simplified human-body phantoms as well as the XCAT, using a custom-developed toy Monte Carlo (MC) and the Geant 4 Application for Tomographic Emission (GATE) simulation tool. The study demonstrates how the probability of photon absorption depends on the decay point and develops absorption maps for $2\gamma$ and $3\gamma$ annihilations, forming the basis for attenuation maps necessary for PET images corrections.

# METHODS

In this study, the gamma quanta absorption in various materials was evaluated using a toy MC simulation developed in the ROOT v6.26/10 data analysis framework [41], as well as with the GATE v9.0 simulation toolkit [42], based on Geant v4 10.7.4 [43]. The simulations were carried out using simplified phantoms approximating the human body and a detailed mesh50_XCAT human phantom. The descriptions of the simulation procedures and used phantoms are presented in the next subsections.

## Toy MC simulation

A key aspect of the toy MC simulations was the generation of the p-Ps and o-Ps decays, with kinematic constraints taken into account. The p-Ps decayed into two photons, and o-Ps decayed into three photons, were simulated. In this work we study the attenuation of photons in the imaged object, which is the same for photons originating from p-Ps $\rightarrow 2\gamma$ decay and direct electron--positron annihilation into $2\gamma$. Similarly, the attenuation of photons from o-Ps $\rightarrow 3\gamma$ decay is the same as that of photons from the direct electron-positron annihilation into $3\gamma$.

In the case of p-Ps, two gamma-quanta emitted, back-to-back, each with the energy $E$ = 511 keV, were generated. The decay simulation consisted of a random selection of the first photon's momentum direction ($\vec{k}_1$) uniformly over the solid angle, with a fixed momentum magnitude of 511 keV. The sphere was parametrised by two angles: the polar angle $\theta$ defined as the angle between the radial vector and the polar axis, and azimuthal angle $\varphi$, which represents the rotation of the radial vector around the polar axis. The random direction was generated by sampling $\varphi \in [0, 360)°$ and $\cos(\theta) \in [-1,1]$. According to the momentum conservation rule, the direction of the second photon's momentum vector was set to $\vec{k}_2 = -\vec{k}_1$.

For the o-Ps decay into three photons (schematically shown in Fig. 1.), its dynamics is described with matrix element $M_{o\text{-}Ps\rightarrow 3\gamma}$, defined by non-relativistic quantum electrodynamics (NRQED) [44] as:

$$M_{o-Ps\rightarrow 3\gamma} = \left(\frac{m_e - E_1}{E_2 E_3}\right)^2 + \left(\frac{m_e - E_2}{E_1 E_3}\right)^2 + \left(\frac{m_e - E_3}{E_1 E_2}\right)^2, \quad (1)$$

where $m_e$ is electron mass and $E_1$, $E_2$, $E_3$ are the energies of the gamma quanta.

In the simulation, the photons' energies are randomised as follows:

$$\begin{aligned} E_1 &\in (0, 511\ \text{keV}), \\ E_2 &\in (511\ \text{keV} - E_1, 511\ \text{keV}), \\ E_3 &= M_{Ps} - E_1 - E_2, \end{aligned} \quad (2)$$

where $M_{Ps}$ = 1022 keV is the positronium mass.

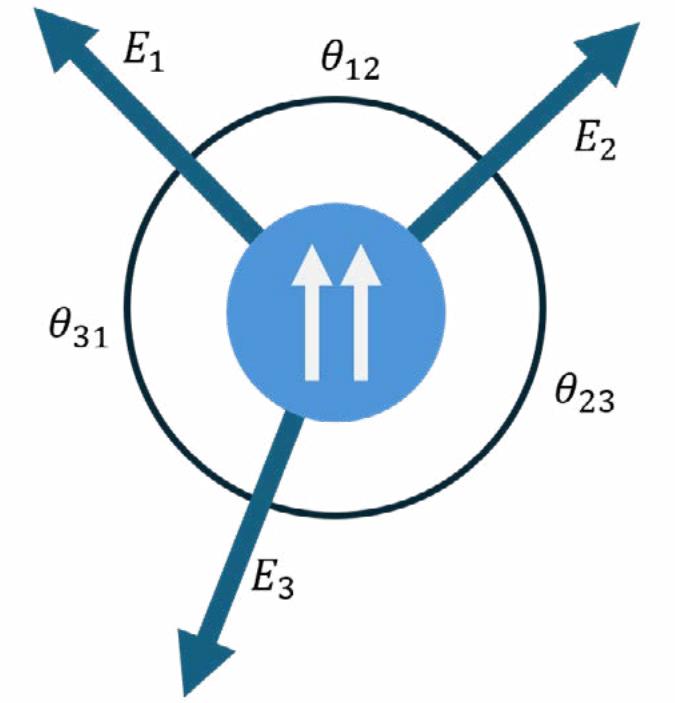


**Fig. 1.** Schematic illustration of the o-Ps decay.

The relative angle between two photons in the decay plane $\theta_{ij}$ was determined based on energy-momentum conservation. For massless photons, where $E_i = p_i$, the relations are as follows:

$$\theta_{ij} = \cos^{-1}\left(\frac{p_k^2 - p_i^2 - p_j^2}{2p_i p_j}\right). \quad (3)$$

The decay plane is then rotated in the three-dimensional frame of reference by applying a random rotation matrix, generated by using a method based on the uniform sampling of unit quaternions [45].

Generated events are accepted or rejected using the MC hit--or-miss method, with a weight specified by the matrix element Equation (1). The results of the simulation are presented in Fig. 2. Panel (A) shows the energy distribution of a photon from the o-Ps decay, while panels (B, C) present Dalitz plots in energy and angular representations. The Dalitz plots describe the kinematics of the decay using two independent parameters, e.g., photons energies ($E_1$, $E_2$) or the relative angles between them ($\theta_{12}$, $\theta_{23}$) [46].

After the positronium decay, a photon can interact with the surrounding material's electrons, nuclei or atoms. The interactions lead to loss of gamma quantum energy or changes in its direction of movement. The dominant processes of interaction, where photons lose part or all of their energy, are the photoelectric effect, Compton scattering and pair production [47]. Summarily, these effects are included in the linear attenuation coefficient $\mu(E)$,which describes the fraction of attenuated gamma quanta from a monoenergetic beam per unit thickness of a material. The probability that gamma quantum with the energy $E$ is not absorbed over distance $d$ in the material takes the following form:

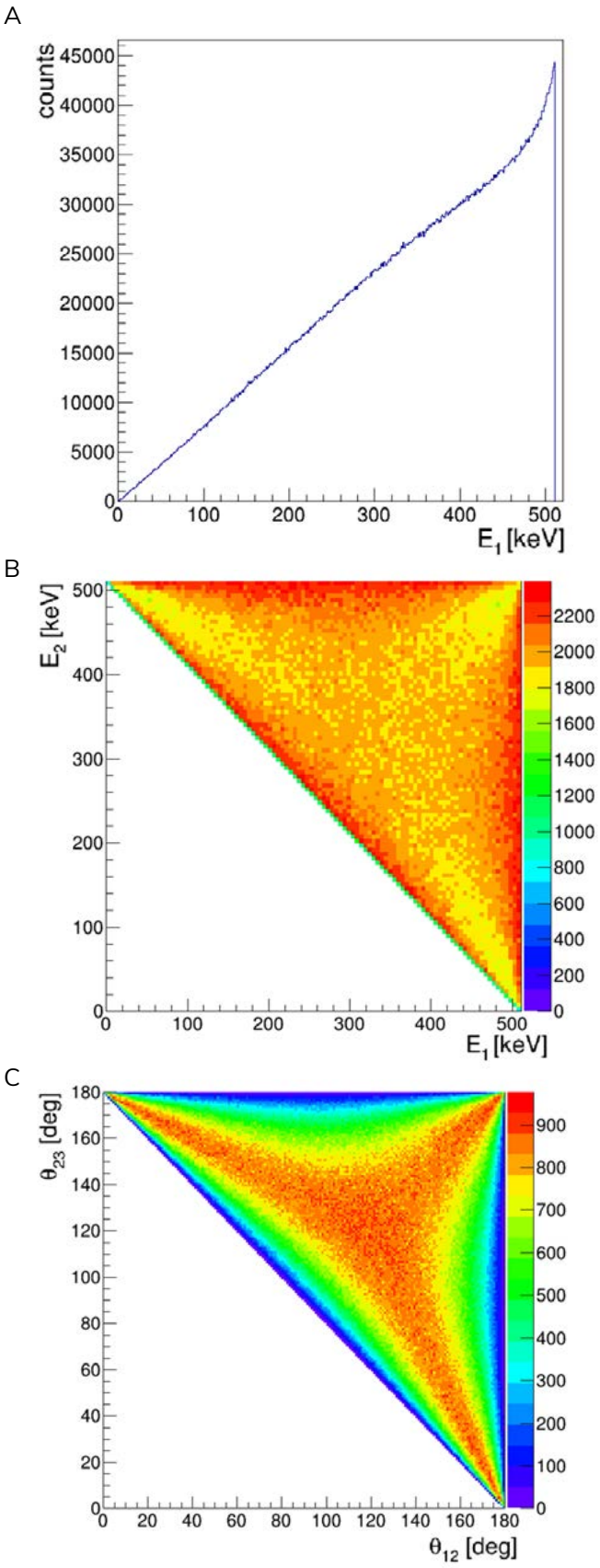


**Fig. 2.** Results of the o-Ps→3γ decay simulation generated for $10^7$ events. (A) Photon energy distribution; (B) Dalitz plot in energy representation; (C) Dalitz plot in angular representation.

$$P = e^{-\mu(E)d}. \quad (4)$$

For a photon passing through m different materials, the escape probability is the product of the individual transmission probabilities: $P_i = \prod_m e^{-\mu_m (Ei) d_m}$. The total probability that all photons from a positronium decay pass through the material is then $P_{tot} = \prod_i P_i$. To determine whether a given gamma quanta pair or triplet escapes the phantom, a MC hit-or-miss method is applied using a weight specified with the probability $P_{tot}$. The toy MC simulations were performed by generating $10^7$ of p-Ps and o-Ps decays in simplified human-body models, described later.

## GATE simulations

Similar simulations were performed using the GATE v9.0 simulation toolkit [42] with the em_livermore_polar physics list, standard for J-PET MC simulations [48]. In the studies, the $\beta^+$ source decay was not directly simulated. p-Ps was represented as back-to-back photon pairs, while o-Ps was simulated using ExtendedVSource extension [42].

The GATE simulations were performed using simple phantom models as well as the XCAT human model, described in the next subsections. No explicit PET detector geometry was implemented in the simulation, as the primary focus of this study was the absorption of photons within the phantom models. Instead, the phantom volumes themselves were defined as crystalSD sensitive detectors, allowing the recording of all photon interactions within the simulated models.

The crystalSD sensitive detector in GATE records detailed information about particle interactions occurring inside a specified volume [42]. This approach was chosen to enable the analysis of photon interactions within the phantom models independently of a specific detector design.

## Simple phantom models

The toy MC and Gate simulations were performed for different models approximating the human body. In the simplest model, the human brain was approximated by a sphere with water, with a radius calculated from volume of the average size of the brain from Ref. [49], equalling 7 cm (Fig. 3A.), while the body was approximated by a cylinder with water with a radius and height of 15 cm and 150 cm, respectively (Fig. 3B.). A more complicated head model consisted of a sphere with brain tissue with a radius of 7 cm surrounded by a 0.655-cm-thick layer of bone (Fig. 3C.).

The properties of the materials included in the simplified human--body model are presented in Tab. I. The values of mass attenuation coefficients of used materials were acquired from the NIST Standard Reference Database 126 [50], while the linear attenuation coefficients were calculated as:

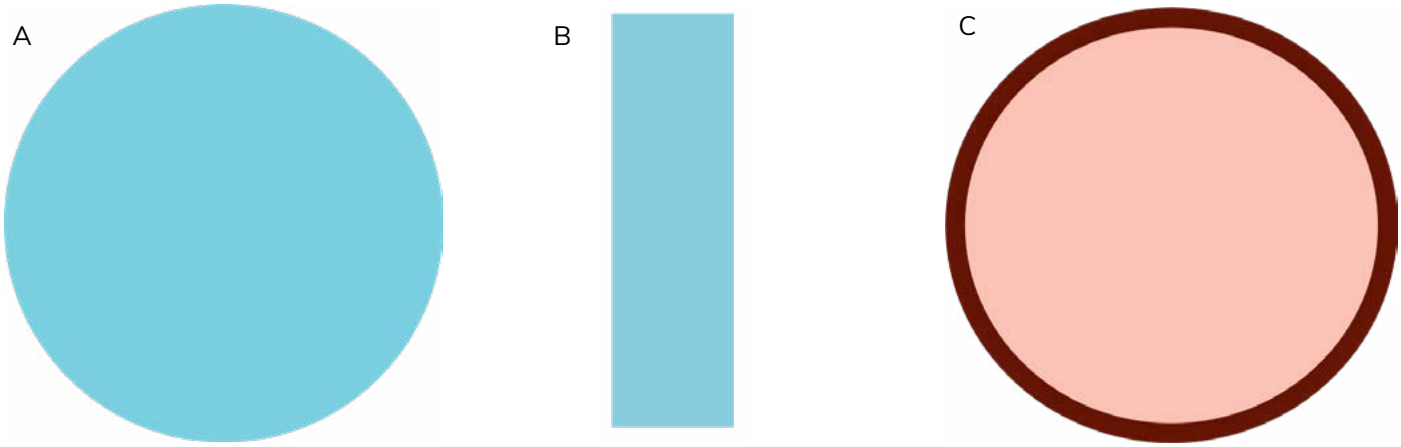


**Fig. 3.** Simplified phantom models. (A) Water sphere; (B) Water cylinder; (C) Head model.

**Tab. I.** Materials used in the toy MC and GATE simulations, and their densities [42].

| MATERIAL NIST STANDARD REFERENCE DATABASE (TOY MC) | MATERIAL GATE MATERIAL DATABASE | DENSITY [g/cm$^3$] |
|---|---|---|
| Water, liquid | Water | 1.00 |
| Bone, cortical | Skull | 1.61 |
| Brain, grey/white matter | Brain | 1.04 |

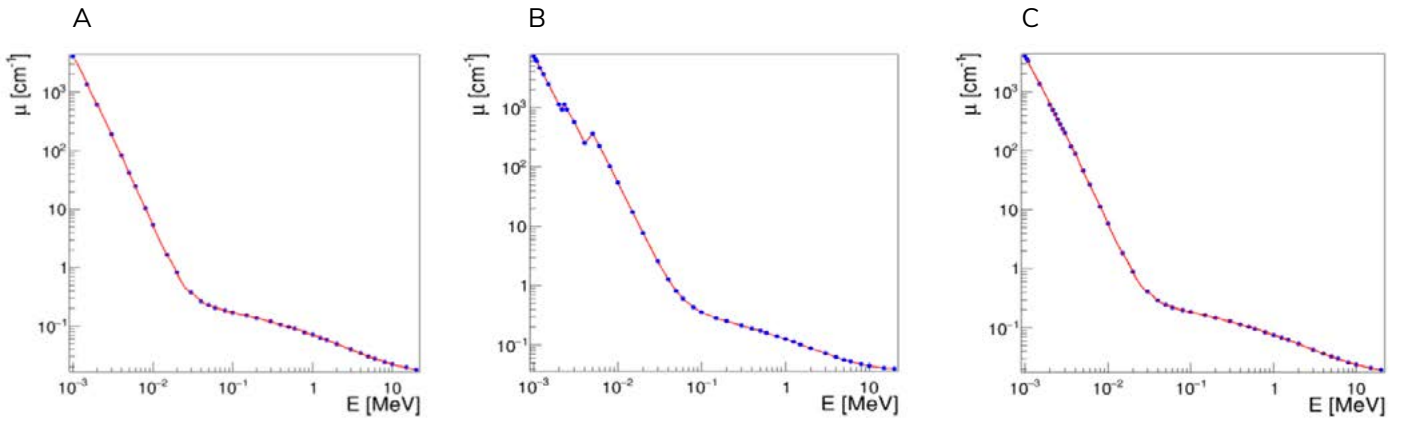


**Fig. 4.** Linear attenuation coefficients of the materials used in the toy MC simulation as a function of photon energy. The points represent the values of linear attenuation coefficients calculated for the values available in NIST Standard Reference Database 126, and the line corresponds to the interpolation. (A) Water, liquid; (B) Bone, cortical; (C) Brain, grey/white matter.

$$\mu = \rho\mu_{mass}, \tag{5}$$

where $\rho$ is the material density. The materials were assigned densities according to the GATE material database [42].

To perform a toy MC simulation of the absorption of gamma quanta originating from o-Ps decays, a continuous distribution of the linear attenuation coefficient was needed. However, since the data from the NIST Standard Reference Database 126 are available only for discrete energy values, interpolation was performed for water, brain and bone tissues, as shown in Fig. 4.

The simulations were performed for both, p-Ps and o-Ps decays, uniformly distributed within the model.

## XCAT phantom model

Using the GATE simulation toolkit, more advanced simulations were performed for a realistic human-body XCAT phantom. In this study, a mesh50_XCAT phantom, developed and maintained by Auer Benjamin, was used (Fig. 5.) [51, 52]. The mesh50_XCAT phantom represents a 50$^{th}$ percentile American male, meaning

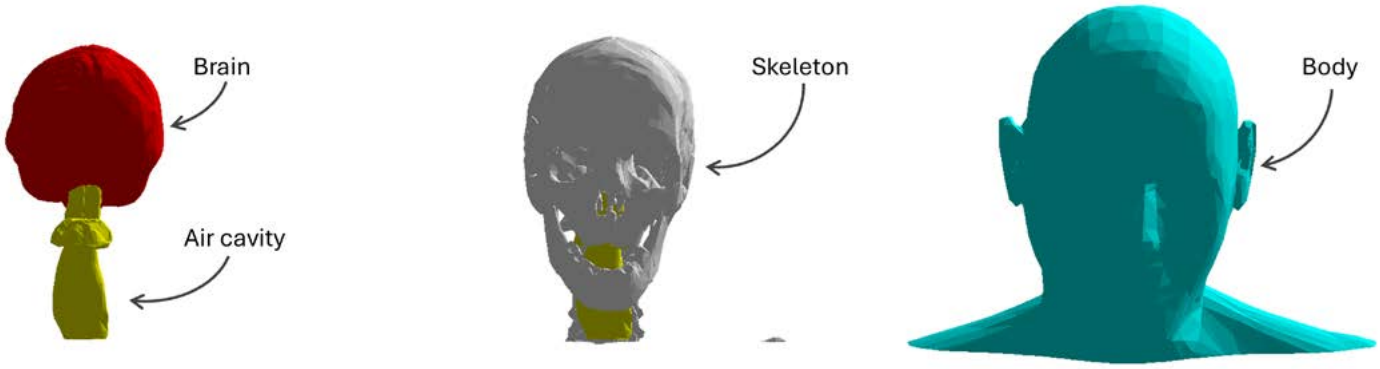


**Fig. 5.** Detailed view of the human-body mesh50_XCAT Phantom [51, 52].

**Tab. II.** Components of the mesh50_XCAT phantom and their materials [51, 52] with their densities [42].

| PHANTOM COMPONENT | MATERIAL | DENSITY [g/cm$^3$] |
|---|---|---|
| Body | Water | 1.00 |
| Air cavity | Air | $1.29 \cdot 10^{-3}$ |
| Brain | Brain | 1.04 |
| Skeleton | SpineBone | 1.42 |

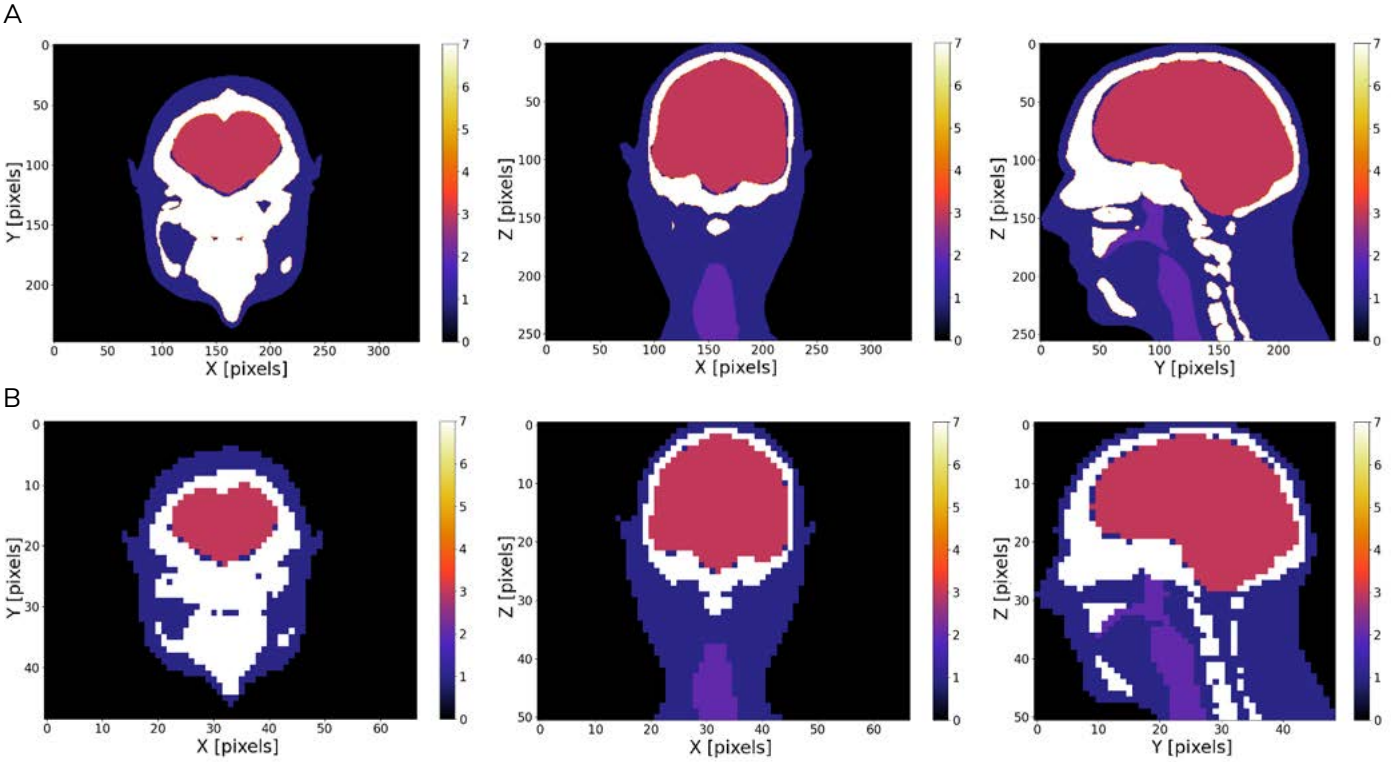


**Fig. 6.** Voxelised versions of the mesh50_XCAT phantom; white denotes bone, pink – brain, blue – water, purple – air. (A) Voxel dimensions of (1, 1, 1) mm$^3$; (B) Voxel dimensions of (5, 5, 5) mm$^3$.

that its body measurements (height, weight and major circumferences) correspond to the median values in the PeopleSize anthropometric database for U.S. adult males [53]. For the purpose of this work, a head-only model was implemented. The individual components of the phantom structure, and their assigned materials from the GATE material database, are presented in Tab. II.

As a uniformly distributed source of p-Ps, a voxelised version of the phantom was used with voxel dimensions of 1 x 1 x 1 mm$^3$ (Fig. 6A.). The simulation with p-Ps consisted of $10^7$ events.

Due to the fact that the GATE v9.0 does not allow use of the voxelised source type and the ExtendedVSource library

simultaneously, o-Ps decays were simulated in a loop. To perform the simulations, a voxelised source was resampled into voxels with the dimensions of 5 x 5 x 5 $mm^3$ (Fig. 6B.). This resampling was performed to reduce the overall computational time by limiting the number of independent sources to be simulated. Each of the 44,350 voxels was simulated as a singular cubic source of o-Ps, and each simulation consisted of $10^3$ events.

## RESULTS

The simulations allowed investigation of the percentage of non-absorbed photon pairs (p-Ps) and triplets (o-Ps) relative to generated events in the phantom models. The numerical results are presented in Tab. III. Only the photon multiplets from which none of the particles reacted in the phantom (e.g., by the photoelectric or Compton effect) were considered as non-absorbed. Statistical uncertainties are negligible due to the high statistics of simulated samples of $10^7$ events.

The results obtained from the toy MC and GATE show good overall agreement. Minor differences can be attributed to differences in the implemented linear attenuation coefficients.

Additionally, absorption maps were generated. These provide emission-point-specific information about the fraction of photon multiplets emitted from a given volume in the phantom, for which at least one gamma quantum interacted with a model's material. Example absorption maps obtained from GATE simulation

**Tab. III.** Percentages of non-absorbed gamma quanta pairs (p-Ps) and triplets (o-Ps) from toy MC and GATE simulations for different phantom models.

| PHANTOM | NON-ABSORBED GAMMA QUANTA MULTIPLETS [%] | | | |
|---|---|---|---|---|
| | p-Ps (2γ) TOY MC | p-Ps (2γ) GATE | o-Ps (3γ) TOY MC | o-Ps (3γ) GATE |
| Water sphere | 37.8 | 37.9 | 18.1 | 18.2 |
| Water cylinder | 7.6 | 7.6 | 1.6 | 1.6 |
| Head model | 30.2 | 30.1 | 11.9 | 11.9 |
| Mesh50_XCAT | – | 24.9 | – | 10.3 |

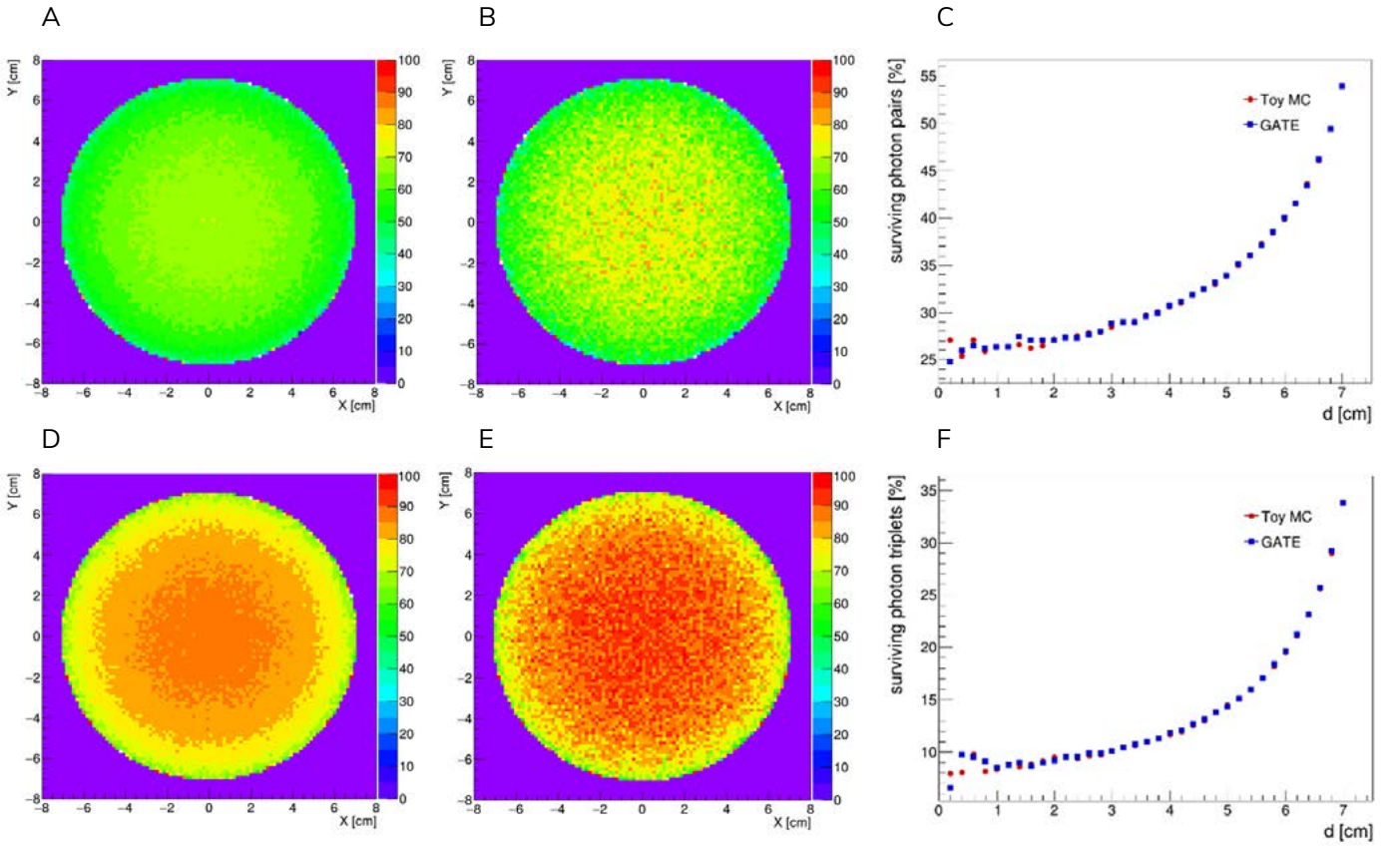


**Fig. 7.** Absorption maps of the water sphere phantom (Fig. 3A.) for positronium decays. The maps are presented as a projection onto an XY plane (A, D), 0.5-cm central slice (B, E), obtained from the GATE simulation, and 1D absorption maps obtained from both toy MC and GATE simulations (C, F). (A) p-Ps (2γ) absorption map – projection; (B) p-Ps (2γ) absorption map – 0.5 cm slice; (C) 1D p-Ps (2γ) absorption map; (D) o-Ps (3γ) absorption map – projection; (E) o-Ps (3γ) absorption map – 0.5 cm slice; (F) 1D o-Ps (3γ) absorption map.

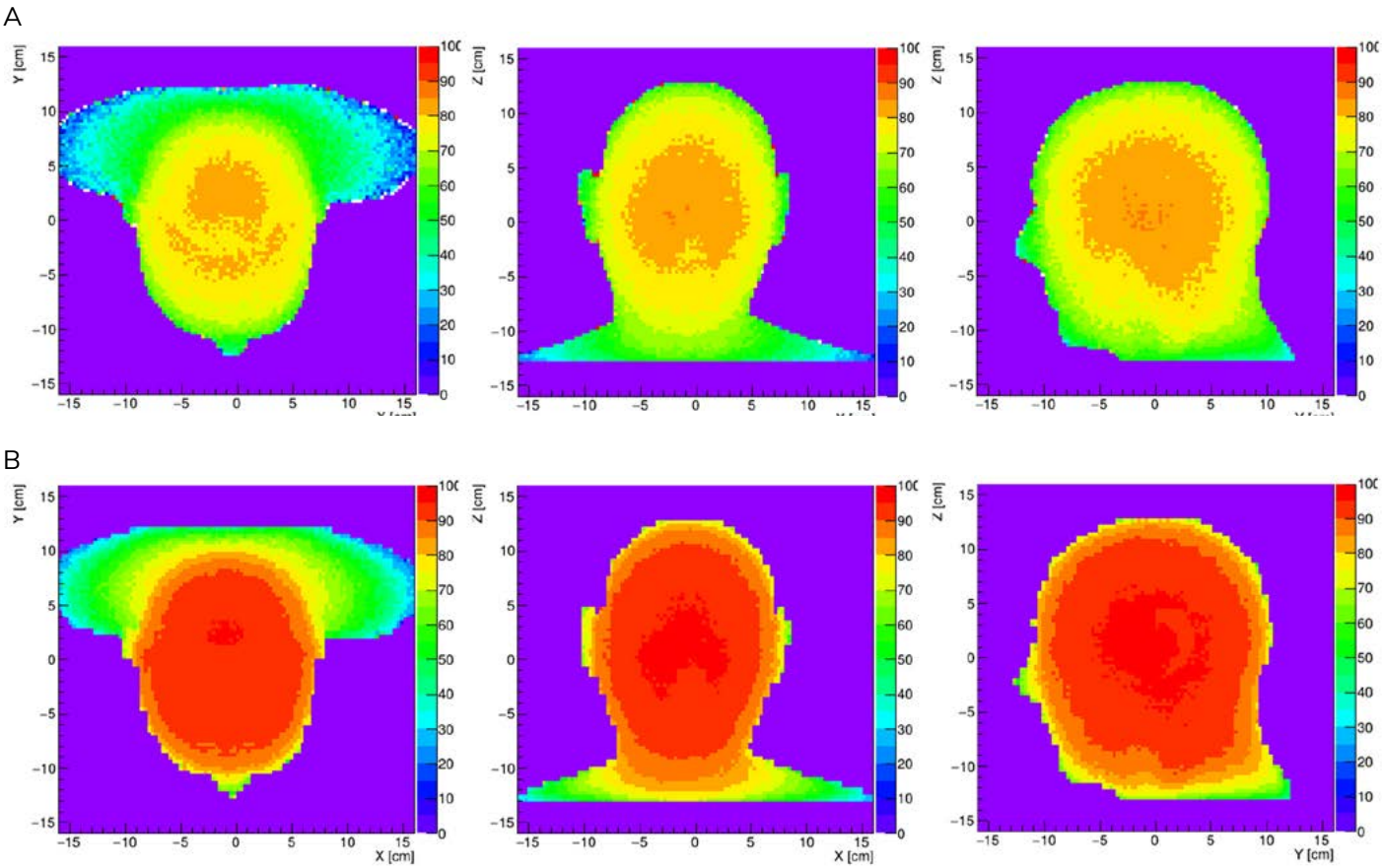


**Fig. 8.** Absorption maps in the coronal transverse and sagittal planes of the XCAT human-body phantom (Fig. 4.), obtained from the GATE simulation. (A) p-Ps (2γ) absorption maps; (B) o-Ps (3γ) absorption maps

corresponding to the water sphere model are presented in Fig. 7., and to the mesh50_XCAT phantom in Fig. 8. The maps represent a full projection of the entire model onto a single plane, as well as a central slice with a thickness of 0.5 cm within ± 0.25 cm from 0 along the axis perpendicular to the given plane.

Furthermore, the percentage of surviving photon multiplets was calculated as a function of the distance between the decay point and the centre of the model for spherical phantoms. The plots were compared between the toy MC and GATE simulations. The results obtained for the water sphere model are presented in Fig. 7C. and 7F. The graphs did not reveal any significant differences between the simulations performed with the two tools, confirming the correctness of the toy MC implementation.

The numerical results, along with the absorption maps, indicate that the absorption of photons produced in three-body decays is significantly higher than that of photons from two-body decays. This observation is consistent with expectations, not only due to the lower energy of each photon in the three-body decay, which leads to a higher linear attenuation coefficient, but also due to the increased probability that at least one gamma quantum will be absorbed in a photon triplet compared to a photon pair. The overall ratio of unabsorbed photon multiplets from 3γ/2γ decays ranges from 1/4 to about 1/2, depending on the phantom (lower for the cylindrical model and higher for the head models). As expected, for the cylindrical phantom simulating the human torso, the attenuation of both 2γ and 3γ photons is higher than in the head phantoms, amounting to approximately 92.5% and 98.4%, respectively.

## CONCLUSIONS

The aim of this study was to investigate the absorption of gamma quanta originating from p-Ps →2γ and o-Ps →3γ decays within various phantoms. The analysis was based on simulations of these decay processes and the photon interactions with matter, performed using two simulation tools: a custom developed toy MC algorithm implemented with the ROOT data analysis framework, and GATE (Geant4 Application for Tomographic Emission). Simulations were carried out using both simplified human-body models and the anatomically detailed mesh50_XCAT human phantom. Within the scope of this work, the ratios of gamma quanta multiplets, from which none of the photons interacted in the phantom was calculated for sources, were distributed uniformly within the phantoms. The key outcome of this study, however, was the generation of absorption maps that provide emission-point-specific information on gamma quantum absorption. These maps form the foundation for constructing attenuation maps (μ-maps), which are essential for tomographic image correction, particularly for three-gamma images. Such μ-maps have not yet been developed for three-gamma imaging,

which remains challenging due to the more complex, energy--dependent kinematics.

## ACKNOWLEDGEMENTS AND FUNDING

We acknowledge support from and the National Science Center through grant nos. 2021/42/A/ST2/00423, 2021/43/B/ST2/02150 and 2022/47/I/NZ7/03112, European Union within the Horizon Europe Framework Programme (ERC Advanced Grant POSITRONIUM no. 101199807), the SciMat and qLife Priority Research Areas budget under the program Excellence Initiative  Research University at Jagiellonian University, the Research Support Module as part of the Excellence Initiative – Research University program at Jagiellonian University and the Polish high-performance computing infrastructure PLGrid (HPC Center: ACK Cyfronet AGH) for providing computer facilities and support within computational grant nos. PLG/2024/017688 and PLG/2025/018762.

## CONFLICT OF INTEREST

The authors have no potential conflicts of interest to declare.

## DATA AVAILABILITY

The simulation data that support the findings of this study are available from the corresponding author upon request.

## REFERENCES

1. Bass SD, Mariazzi S, Moskal P, Stępień E. Colloquium: Positronium physics and biomedical applications. Rev. Mod. Phys. 2023;95(2):02102. doi: https://doi.org/10.1103/RevModPhys.95.021002.2.
2. Moskal P, Jasińska B, Stępień EŁ, Bass SD. Positronium in medicine and biology. Nat Rev Phys. 2019;1(9):527–9. doi: https://doi.org/10.1038/s42254-019-0078-7.
3. Moskal P. Positronium Imaging. In: 2019 IEEE Nuclear Science Symposium and Medical Imaging Conference (NSS/MIC); 2019 Oct 26–Nov 02; Manchester, UK. IEEE; 2019. p. 1–3. doi: https://doi.org/10.1109/NSS/MIC42101.2019.9059856.
4. Moskal P, Kisielewska D, Curceanu C, Czerwiński E, Dulski K, Gajos A, et al. Feasibility study of the positronium imaging with the J-PET tomograph. Phys Med Biol. 2019;64(5):055017. doi: https://doi.org/10.1088/1361-6560/aafe20.
5. Moskal P, Kisielewska D, Shopa R, Bura Z, Chhokar J, Curceanu C, et al. Performance assessment of the 2 γpositronium imaging with the total--body PET scanners. EJNMMI Phys. 2020;7(1):44. doi: https://doi.org/10.1186/s40658-020-00307-w.
6. Moskal P, Dulski K, Chug N, Curceanu C, Czerwiński E, Dadgar M, et al. Positronium imaging with the novel multiphoton PET scanner. Sci Adv. 2021;7(42):eabh4394. doi: https://doi.org/10.1126/sciadv.abh4394.
7. Moskal P, Baran J, Bass S, Choiński J, Chug N, Curceanu C, et al. Positronium image of the human brain in vivo. Sci Adv. 2024;10(37):eadp2840. doi: https://doi.org/10.1126/sciadv.adp2840.
8. Vandenberghe S, Moskal P, Karp JS. State of the art in total body PET. EJNMMI Physics. 2020 May 25;7(1):35. doi: https://doi.org/10.1186/s40658-020-00290-2.
9. Korcyl G, Moskal P, Bednarski T, Białas P, Czerwiński E, Kapłon Ł, et al. Trigger-less and reconfigurable data acquisition system for positron emission tomography. Bio-Algorithms and Med-Systems. 2014;10:37–40. doi: https://doi.org/10.1515/bams-2013-0115.
10. Das M, Mryka W, Beyene EY, Parzych S, Sharma S, Stępień E, et al. Estimating the efficiency and purity for detecting annihilation and prompt photons for positronium imaging with J-PET using toy Monte Carlo simulation. Bio-Algorithms and Med-Systems. 2023;19(1):87–95. doi: https://doi.org/10.5604/01.3001.0054.1938.
11. Das M, Reimund B, Sharma S, Parzych S, Niedźwiecki S, Badawi R, et al. Development of correction techniques for the J-PET Scanner. Bio--Algorithms and Med-Systems. 2024;20:1–8. doi: https://doi.org/10.5604/01.3001.0054.9362.
12. Das M, Sharma S, Bilewicz A, Choiński J, Chug N, Curceanu C, et al. First positronium imaging using 44Sc with the J-PET scanner: a case study on the NEMA-Image Quality phantom. arXiv:2506.07230. doi: https://doi.org/10.48550/arXiv.2506.07230.
13. Jasińska B, Moskal P. A New PET Diagnostic Indicator Based on the Ratio of 3γ/2γ Positron Annihilation. Acta Phys. Pol. B. 2017;48:1577. doi: https://doi.org/10.5506/APhysPolB.48.1577.
14. Moskal P, Gajos A, Mohammed M, Chhokar J, Chug N, Curceanu C, et al. Testing CPT symmetry in ortho-positronium decays with positronium annihilation tomography. Nat Commun. 2021;12(1):5658. doi: https://doi.org/10.1038/s41467-021-25905-9.
15. Tashima H, Yamaya T. Three-Gamma Imaging in Nuclear Medicine: A Review. IEEE Trans. Radiat. Plasma Med. Sci. 2024;8(8):85366. doi: https://doi.org/10.1109/TRPMS.2024.3470836.
16. Takyu S, Nishikido F, Tashima H, Akamatsu G, Matsumoto K, Takahashi M, et al. Positronium lifetime measurement using a clinical PET system for tumor hypoxia identification. Nucl. Instrum. Methods Phys. Res. A. 2024;1065:169514. doi: https://doi.org/10.1016/j.nima.2024.169514.
17. Takyu S, Shibuya K, Nishikido F, Tashima H, Takahashi M, Yamaya T. Two-dimensional positronium lifetime imaging using certified reference materials. Appl Phys Express. 2022;15(10):10601. doi: https://doi.org/10.35848/1882-0786/ac8d7b.1.
18. Takyu S, Ikeda H, Wakizaka H, Nishikido F, Matsumoto K, Tashima H, et al. Positron annihilation lifetime measurement with TOF-PET detectors: feasibility of Iodine-124 use. Appl Phys Express. 2023;16(11):11601. doi: https://doi.org/10.35848/1882-0786/ad047c.
19. Mercolli L, Steinberger WM, Grundler PV, Moiseeva A, Braccini S, Conti M, et al. First positronium lifetime imaging with scandium-44 on a long axial field-of-view PET/CT. Front Nucl Med. 2025;5:1648621. doi: https://doi.org/10.3389/fnume.2025.1648621.
20. Mercolli L, Steinberger WM, Rathod N, Conti M, Moskal P, Rominger A, et al. Phantom imaging demonstration of positronium lifetime with a long axial field-of-view PET/CT and 124I. EJNMMI Phys. 2025;12(1):80. doi: https://doi.org/10.1186/s40658-025-00790-z.
21. Huang B, Wang Z, Zeng X, Goldan AH, Qi J. Fast high-resolution lifetime image reconstruction for positron lifetime tomography. Commun Phys. 2025;8(1):181. doi: https://doi.org/10.1038/s42005-025-02100-6.
22. Huang B, Li T, Arino-Estrada G, Dulski K, Shopa RY, Moskal P, et al. SPLIT: Statistical Positronium Lifetime Image Reconstruction via Time-

-Thresholding. IEEE Trans Med Imaging. 2024;43(6):2148–58. doi: https://doi.org/10.1109/TMI.2024.3357659.

23. Qi J, Huang B. Positronium Lifetime Image Reconstruction for TOF PET. IEEE Trans Med Imaging. 2022;41(10):2848–55. doi: https://doi.org/10.1109/TMI.2022.3174561.

24. Steinberger WM, Mercolli L, Breuer J, Sari H, Parzych S, Niedzwiecki S, et al. Positronium lifetime validation measurements using a long-axial field-of--view positron emission tomography scanner. EJNMMI Phys. 2024;11(1):76. doi: https://doi.org/10.1186/s40658-024-00678-4.

25. Huang B, Qi J. High-resolution positronium lifetime tomography by the method of moments. Phys Med Biol. 2024;69(24):24NT01. doi: https://doi.org/10.1088/1361-6560/ad9543.

26. Huang HH, Zhu Z, Booppasiri S, Chen Z, Pang S, Kao CM. A Statistical Reconstruction Algorithm for Positronium Lifetime Imaging Using Time--of-Flight Positron Emission Tomography. IEEE Trans. Radiat. Plasma Med. Sci. 2025;9(4):478–86. doi: https://doi.org/10.1109/trpms.2025.3531225.

27. Chen Z, An L, Kao CM, Huang HH. The properties of the positronium lifetime image reconstruction based on maximum likelihood estimation. Bio-Algorithms and Med-Systems. 2023;19(1):1–8. doi: https://doi.org/10.5604/01.3001.0054.1807.

28. Berens L, Hsu I, Chen CT, Halpern H, Kao CM. An analytic, moment-based method to estimate orthopositronium lifetimes in positron annihilation lifetime spectroscopy measurements. Bio-Algorithms and Med-Systems. 2024;20:40–8. doi: https://doi.org/10.5604/01.3001.9141.

29. Kacperski K, Spyrou NM, Smith FA. Three-gamma annihilation imaging in positron emission tomography. IEEE Trans. Med. Imaging. 2004;23(4):525–9. doi: https://doi.org/10.1109/TMI.2004.824150.

30. Kacperski K, Spyrou NM. Three-gamma annihilations as a new modality in PET. IEEE Nucl Sci Symp Conf Rec. 2004;6:3752–6. doi: https://doi.org /10.1109/NSSMIC.2004.1466696.

31. Kacperski K, Spyrou NM. Performance of three-photon PET imaging: Monte Carlo simulations. Phys. Med. Biol. 2005;50:5679. doi: https://doi.org/10.1088/0031-9155/50/23/019.

32. Abuelhia E, Kacperski K, Kafala S, Spyrou NM. Performance of triple coincidence imaging as an addition to dedicated PET. Radiat. Phys. Chem. 2007;76(2):351–6. doi: https://doi.org/10.1016/j.radphyschem.2006.03.066.

33. Abuelhia E, Kacperski K, Spyrou NM. Three-photon annihilation in PET: 2D imaging experiments. J Radioanal Nucl Chem. 2007;271:489–95. doi: https://doi.org/10.1007/s10967-007-0235-9.

34. Abuelhia E, Alzimami K, Alkhorayef M, Podolyak Z, Spyrou NM. Measurement of coincidence timing resolution of scintillation detectors compared to semiconductor detectors to image three-photon positron annihilation. J Radioanal Nucl Chem 2008; 278:767–771. doi: https://doi.org/10.1007/s10967-008-1608-4.

35. Yu Z, Asch H, Gerber R, Redey A, Starosta K, Tam D, et al. Novel application of the 8π gamma-ray spectrometer for 3γ positron emission tomography. Nucl. Instrum. Methods Phys. Res. A. 2026;1084:171168. doi: https://doi.org/10.1016/j.nima.2025.171168.

36. Alkhorayef M, Sulieman A, Alsager OA, Alrumayan F, Alkhomashi N. Investigation of using positronium and its annihilation for hypoxia PET imaging. Radiat. Phys. Chem. 2021;188:109690. doi: https://doi.org/10.1016/j.radphyschem.2021.109690.

37. Fujimoto M, Shimazoe K, Sato R, Hamdan M, Uenomachi M, Stephenson L, et al. Advancing PET through Direct Imaging of Three-Photon Decay using Pure Positron Emitters [Preprint]. 2025 [cited Dec 23]: [1 p.]. Available from: https://doi.org/10.21203/rs.3.rs-7272322/v1.

38. Carney JPJ, Townsend DW, Rappoport V, Bendriem B. Method for transforming CT images for attenuation correction in PET/CT imaging. Med Phys. 2006;33(4):976–3. doi: https://doi.org/10.1118/1.2174132.

39. Ay MR, Sarkar S. Computed tomography based attenuation correction in PET/CT: Principles, instrumentation, protocols, artifacts and future trends. Iran J Nucl Med. 2007;15(2):1–29.

40. Adkins GS. Analytic evaluation of the amplitudes for orthopositronium decay to three photons to one-loop order. Phys Rev Lett. 1996;76(26):4903–6. doi: https://doi.org/10.1103/PhysRevLett.76.4903.

41. Brun R, Rademakers F. ROOT – An object oriented data analysis framework. Nucl. Instrum. Methods Phys. Res. A. 1997;389(1):81–6. doi: https://doi.org/10.1016/S0168-9002(97)00048-X.

42. Jan S, Santin G, Strul D, Staelens S, Assié K, Autret D, et al. GATE: a simulation toolkit for PET and SPECT. Phys Med Biol. 2004;49(19):4543–61. doi: https://doi.org/10.1088/0031-9155/49/19/007.

43. Agostinelli S, Allison J, Amako K, Apostolakis J, Araujo H, Arce P, et al. Geant4 – a simulation toolkit. Nucl. Instrum. Methods Phys. Res. A. 2003;506:250–303. doi: https://doi.org/10.1016/S0168-9002(03)01368-8.

44. Landau LD, Lifshitz EM. Quantum mechanics: non-relativistic theory. Oxford: Pergamon; 1958.

45. Shoemake K. III.6 – Uniform random rotations. In: Kirk D, editor. Graphics Gems III (IBM Version). San Francisco: Morgan Kaufmann; 1992. p. 124–32. doi: https://doi.org/10.1016/B978-0-08-050755-2.50036-1.

46. Dalitz RH. CXII. On the analysis of τ-meson data and the nature of the τ-meson. Lond. Edinb. Dubl. Phil. Mag. 1953;44(357):1068–80.

47. Obodovskiy I. Interaction of Gamma Quanta With Matter. In: Obodovskiy I, editor. Radiation. Amsterdam: Elsevier; 2019. p. 137–150. doi: https://doi.org/10.1016/B978-0-444-63979-0.00006-9.

48. Moskal P, Kowalski P, Shopa RY, Raczyński L, Baran J, Chug N, et al. Simulating NEMA characteristics of the modular total-body J-PET scanner-an economic total-body PET from plastic scintillators. Phys Med Biol. 2021;66(17):175015. doi: https://doi.org/10.1088/1361-6560/ac16bd.

49. Bayat P-D, Ghanbari A, Sohouli P, Amiri S, Sari-Aslani P. Correlation of Skull Size and Brain Volume, with Age, Weight, Height and Body Mass Index of Arak Medical Sciences Students. Int. J. Morphol. 2012;30:157–61. doi: https://doi.org/10.4067/S0717-95022012000100028.

50. Hubbell JH, Seltzer SM. Tables of X-Ray Mass Attenuation Coefficients and Mass Energy-Absorption Coefficients from 1 keV to 20 MeV for Elements Z = 1 to 92 and 48 Additional Substances of Dosimetric Interest. Radiation Physics Division, NIST. 1995. doi: https://dx.doi.org/10.18434/T4D01F.

51. Auer B, Könik A, Fromme TJ, De Beenhouwer J, Kalluri KS, Lindsay C, et al. Mesh modeling of system geometry and anatomy phantoms for realistic GATE simulations and their inclusion in SPECT reconstruction. Phys Med Biol. 2023;68(7):07505. doi: https://doi.org/10.1088/1361-6560/acbde2.5.

52. Auer B. Mesh-based-Human-Phantom-for-Simulation [Internet]. [cited 2025 May 13]. Available at: https://github.com/BenAuer2021/Mesh-based-Human-Phantom-for-Simulation.

53. PeopleSize anthropometry database, Open Ergonomics Ltd [Internet]. [cited 2025 Dec 23]. Available at: https://openerg.com/.